

## Non-classical mechanical states guided in a phononic waveguide

Zivari, Amirparsa; Stockill, Robert; Fiaschi, Niccolò; Gröblacher, Simon

**DOI**

[10.1038/s41567-022-01612-0](https://doi.org/10.1038/s41567-022-01612-0)

**Publication date**

2022

**Document Version**

Final published version

**Published in**

Nature Physics

**Citation (APA)**

Zivari, A., Stockill, R., Fiaschi, N., & Gröblacher, S. (2022). Non-classical mechanical states guided in a phononic waveguide. *Nature Physics*, 18(7), 789-793. <https://doi.org/10.1038/s41567-022-01612-0>

**Important note**

To cite this publication, please use the final published version (if applicable). Please check the document version above.

**Copyright**

Other than for strictly personal use, it is not permitted to download, forward or distribute the text or part of it, without the consent of the author(s) and/or copyright holder(s), unless the work is under an open content license such as Creative Commons.

**Takedown policy**

Please contact us and provide details if you believe this document breaches copyrights. We will remove access to the work immediately and investigate your claim.



# Non-classical mechanical states guided in a phononic waveguide

Amirparsa Zivari , Robert Stockill , Niccolò Fiaschi  and Simon Gröblacher  

**The ability to create, manipulate and detect non-classical states of light has been key for many recent achievements in quantum physics and for developing quantum technologies. Achieving the same level of control over phonons, the quanta of vibrations, could have a similar impact, in particular on the fields of quantum sensing and quantum information processing. Here we present a crucial step towards this level of control and realize a single-mode waveguide for individual phonons in a suspended silicon microstructure. We use a cavity-waveguide architecture, where the cavity is used as a source and detector for the mechanical excitations while the waveguide has a free-standing end to reflect the phonons. This enables us to observe multiple round trips of phonons between the source and the reflector. The long mechanical lifetime of almost 100  $\mu\text{s}$  demonstrates the possibility of nearly lossless transmission of single phonons over, in principle, tens of centimetres. Our experiment demonstrates full on-chip control over travelling single phonons strongly confined in the directions transverse to the propagation axis, potentially enabling a time-encoded multimode quantum memory at telecommunications wavelength and advanced quantum acoustics experiments.**

Creating and detecting quantum states of mechanical motion open up new possibilities for quantum information processing, quantum sensing and probing the foundations of quantum physics<sup>1</sup>. In particular, within the field of quantum optomechanics, many remarkable milestones have been reached over the past years, from showing the ability to realize the quantum ground state of a mechanical oscillator and single-phonon control<sup>2</sup>, unambiguous demonstration of the quantum nature of phonons through the creation of entangled states<sup>3–5</sup> and a Bell test<sup>6</sup>, to realizing a long-coherence-time quantum memory<sup>7</sup>. Furthermore, the field has shown the potential to enable crucial applications in connecting quantum computers and transferring information between them<sup>8–11</sup>. While these applications usually rely on highly confined phononic states (with a typical mode volume on the order of the wavelength), the use of travelling phonons promises the ability to create on-chip architectures for classical and quantum information<sup>12</sup>, with the potential to add completely new capabilities compared with their optical counterparts. The exciting prospects in this new field of quantum acoustics are enabled by the orders of magnitude slower propagation speed compared with photons, the inherently low loss, their extremely low energy and the small mode volume compared with gigahertz-frequency photons. These features make phonons ideally suited for direct manipulation on a chip with wavelength-sized components, while the ability to realize significant time delays in a short distance makes this type of system an ideal platform for on-chip operations<sup>13</sup>. Furthermore, phonons have also demonstrated their unique capability to efficiently couple and even mediate the interaction between various quantum systems<sup>14</sup>, such as superconducting qubits<sup>15</sup>, defect centres in solids<sup>16</sup> and quantum dots<sup>17,18</sup>. Using mechanical excitations as low-loss carriers of quantum information will allow for the construction of two-dimensional architectures and large-scale phononic quantum networks<sup>19</sup>.

While the creation of non-classical mechanical states has been demonstrated in multiple physical systems<sup>20</sup>, only a very limited number of experiments have been able to realize propagating modes

in the quantum regime, all based on surface acoustic waves<sup>15,21,22</sup>. This approach comes with its own limitations and challenges, such as relatively short lifetimes, losses due to beam steering and diffraction, typically only bidirectional emission and no full confinement of the mode except in resonators. In the classical domain on the other hand, several proof-of-concept experiments have realized the creation, transport and detection of mechanical states at cryogenic temperatures<sup>23</sup> over millimetre ranges, as well as at room temperature and atmospheric pressure<sup>24</sup>. The possibility of guiding a mechanical quantum state in a waveguide that confines the excitation in all directions transverse to its propagation, similar to optical fibres and waveguides, remains an open challenge.

In this work, we demonstrate a single-mode phononic waveguide directly coupled to an on-chip source and detector for non-classical mechanical states. We verify the non-classicality of the launched mechanical states by measuring their quantum correlations with an optical read-out field. In particular, we use the optomechanical interaction to herald the creation of a single phonon, which then leaks into the phononic waveguide. Since the waveguide has a free-standing end that acts as a mirror for the phonons, the excitations bounce, that is, reflect back and forth with a certain characteristic time that is determined by the group velocity and the length of the waveguide. Moreover, we observe non-classical correlations between time-bin-encoded phonons<sup>25</sup>, by creating and detecting a phonon in either an early or late time window. The long mechanical lifetime of the device will also allow the creation of an on-chip network for quantum acoustic experiments. With the on-chip source, detector and waveguide presented in this work, only a phononic beam splitter and phase modulator need to be developed to achieve full coherent control over phonons on a chip.

We design our phononic crystal waveguide in thin-film silicon, which is single-mode for the symmetric breathing mode of the structure, in the frequency range of interest (at around 5 GHz with a single-mode range of 750 MHz) and has an approximately linear dispersion, to maintain the spatial mode shape of the travelling phonons. This waveguide is connected to an optomechanical resonator

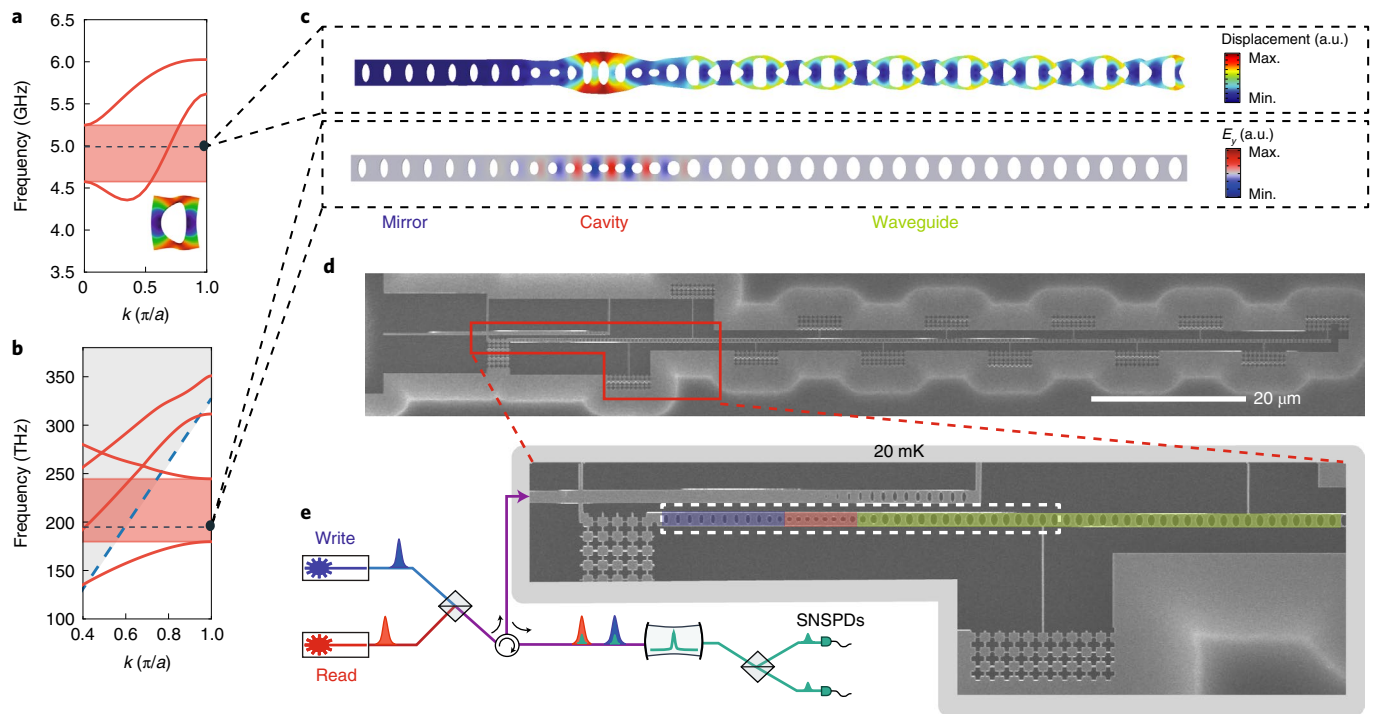


**Fig. 1 | Phononic waveguide design.** **a**, Band diagram for the modes with a symmetric displacement field with respect to the propagation direction along the waveguide. These modes are expected to couple efficiently to the resonant optomechanical cavity mode. The highlighted region (red) shows a single-mode waveguide for the symmetric breathing mode with linear dispersion. The dashed line represents the frequency of the modes of the optomechanical structure. Inset: mode shape of the unit cell from this simulation for the band of interest. **b**, Band diagram for the optical TE mode of the phononic waveguide, exhibiting a band gap at telecommunications wavelengths, allowing for a confined optical mode inside the optomechanical resonator. The dashed blue line is the light cone, with the non-guided modes in the grey-shaded area. **c**, Mechanical (top) and optical (bottom) eigenfrequency simulation of the full cavity and waveguide structure. Clearly visible are the resonant breathing mode of the optomechanical crystal (left) and the waveguide mode (right). As the mechanical mode leaks through the waveguide, the optical mode remains confined inside the optomechanical resonator. **d**, A scanning electron microscopy image of the device used in the experiment, showing the full device with mirror, cavity and the 92- $\mu\text{m}$ -long waveguide, as well as the optical coupling waveguide (top left). **e**, Schematic of the set-up together with a zoomed-in section of **d** (indicated by the red box). The blue, red and green regions show the mirror, cavity and waveguide, respectively. The white dashed rectangle is the area of the simulation in **c**. See the text and SI for more details.

acting as the single-phonon source and detector. For the waveguide design, only the symmetric breathing mode is considered, to enable good mode overlap with the mode of the optomechanical cavity, as these resonant modes have large optomechanical coupling and can easily be created and detected optically. At the same time, to realize a high-finesse optical cavity, we design our phononic waveguide to act as a mirror for photons, therefore confining the optical field in the optomechanical resonator.

The details of our design are shown in Fig. 1a,b, where we plot the band structure with the right mechanical symmetry, as well as the transverse electric (TE)-polarized optical mode. An eigenvalue simulation of the full structure, cavity and waveguide is shown in Fig. 1c. The mechanical mode extends into the waveguide, while the optical mode is strongly confined to the cavity region with a mode volume similar to previous works<sup>4,26–28</sup>. The different sizes of the holes in the structure create the mirror, defect and waveguide. The hole dimensions and periodicity in the waveguide part are adjusted to tune the group velocity. We design the waveguide to have a small group velocity while still having a linear band inside the frequency range of interest (see the Supplementary Information (SI) for more details). From the simulated group velocity, the time duration of the mechanical packet (set by the optical pulse length of 40 ns) and the time of the mechanical excitation to leak from the cavity to the waveguide, we determine a minimum length of about 40  $\mu\text{m}$  for the waveguide for the excitation to completely leave the

cavity before it comes back again, which is why we choose a length of 92  $\mu\text{m}$ . To support the long waveguide after suspension, we use narrow (50-nm-wide) tethers to connect it to the surrounding silicon. Moreover, to prevent any mechanical dissipation through the tethers, they are directly connected to a phononic shield, as seen in the zoomed-in image of the device in Fig. 1e. The phononic shield features a bandgap from 4 to 6 GHz, and by increasing the number of periods in the shields, we can increase the mechanical lifetime (SI). The same phononic shields are used at the left end of the device to further increase the mechanical lifetime.

A picture of the device and sketch of the experimental set-up can be found in Fig. 1d,e. To excite and detect non-classical phonons, we use laser pulses detuned from the optical resonance to address the optomechanical Stokes and anti-Stokes sidebands in order to create (write) the mechanical excitation and map it onto the optical mode (read), respectively<sup>29</sup>. After being combined on a 50:50 beam splitter (BS), the light is routed via an optical circulator to the device. The reflected light from the device is then filtered using free-space Fabry–Pérot cavities to block the pump laser pulses and, after another BS, is sent to the superconducting nanowire single-photon detectors (SNSPDs). The device itself is cooled to 20 mK to initialize the mechanical mode of interest deep in the ground state.

For the initial characterization of the device, we use a tunable continuous-wave laser to determine the optical resonance in reflection. As shown in Fig. 2a, the fundamental optical

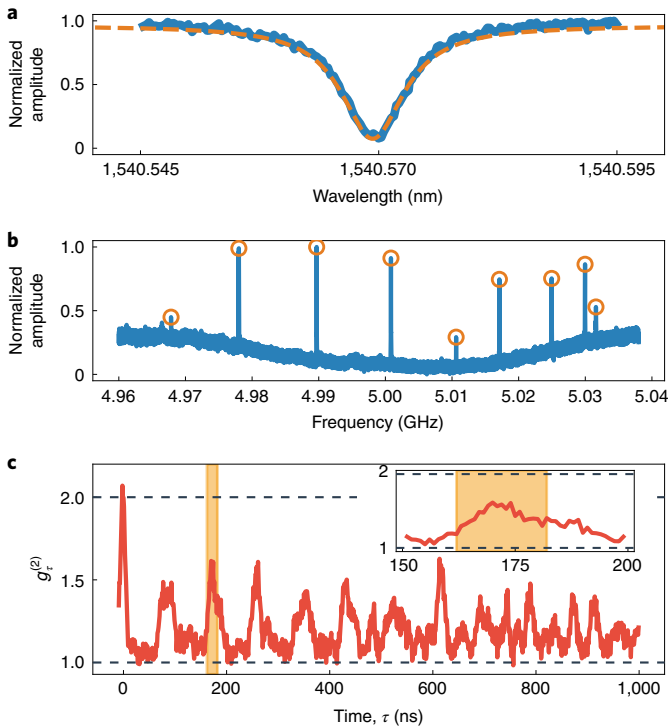


**Fig. 2 | Device characterization.** **a**, Characterization of the optical resonance of the device in reflection, with experimental data in blue and Lorentzian fit in orange. **b**, Mechanical spectrum measured using the optomechanical-induced transparency technique at 20 mK. The series of peaks is given by the hybridization of the cavity mode and the modes of the waveguide (approximately equally spaced). Orange circles highlighting the mechanical eigenmodes. **c**,  $g_r^{(2)}$  of a waveguide-coupled thermal state for different delays between two detection events ( $\tau$ ). Note the series of peaks indicating the back-and-forth travel of phonons in the waveguide. The reduced maxima for these peaks are attributed to the non-constant FSR. The area highlighted in orange is the round-trip peak chosen for the pulsed experiment with single-phonon states and the black dashed lines show the  $g_r^{(2)}$  for uncorrelated events (at 1) and for a thermal state (at 2). Inset: zoom-in around the highlighted area.

resonance has a central wavelength of around 1,541 nm and a line-width of  $\kappa_1 = 1,021$  MHz (with extrinsic and intrinsic loss rates of  $\kappa_e = 364$  MHz and  $\kappa_i = 656$  MHz, respectively). We measure the mechanical spectrum using the optomechanical-induced transparency technique<sup>30</sup> (see SI for details). The resulting renormalized amplitude of the reflected probe field ( $|S_{21}|$ ) is plotted in Fig. 2b, where a series of (almost) equally spaced peaks shows the hybridization of the single mode of the cavity with the series of modes of the free-ended waveguide. We choose the first prominent mechanical resonance (at around 4.98 GHz) as the frequency to which we detune the laser with respect to the optical resonance wavelength for addressing the Stokes and anti-Stokes interaction. We further measure the equivalent single-photon optomechanical coupling rate from the Stokes scattering probability using a short optical pulse with full-width at half-maximum of about 40 ns, obtaining a collective  $g_0/2\pi \approx 460$  kHz (for a detailed explanation, see the SI). This is the joint coupling rate of all mechanical eigenmodes within the detection filter bandwidth.

To determine the time dynamics of the phononic wave packet, we measure the second-order correlation function  $g_r^{(2)}$  of the light scattered from the cavity with a continuous-wave read-out tone detuned to the anti-Stokes sideband. Due to non-negligible

optical absorption in silicon, the continuous laser creates a thermal-mechanical population in the device<sup>31</sup>. In this experiment, the continuous red-detuned laser field excites thermal phonons in a broad frequency range. These phonons are read out by the same red-detuned field, which allows us to measure only the anti-Stokes scattered photons on resonance with the optical cavity. The phononic state is therefore mapped onto the photonic state, and the photons are finally detected using our SNSPDs. As a result, the photon statistics of the optical field corresponds to the phonon statistics of the thermal-mechanical mode. We obtain the  $g_r^{(2)}$  between emitted photons from the device by measuring two-photon coincidences on two different SNSPDs and normalizing them to the single-photon counts of the SNSPDs. Owing to the optomechanical interaction, this is equivalent to measuring the  $g_r^{(2)}$  of the mechanical-thermal states, for different delays between the SNSPDs clicks  $\tau$ . The results are plotted in Fig. 2c, showing an (almost) equally spaced series of peaks. As expected for a thermal state, at  $\tau = 0$ , we observe  $g_r^{(2)} = 2$ , which is then modulated as the state leaks into the waveguide. We attribute the reduced maxima for the round-trip peaks ( $g_r^{(2)} \approx 1.5$  instead of 2) to coupling to undesirable asymmetric mechanical modes (which have relatively low optomechanical coupling rates and thus cannot be detected optically), as well as the non-constant FSR between mechanical modes of the device, which could be caused by the dispersion of the phononic waveguide. The exact effect will require a more detailed theoretical and experimental analysis in the future.

We use three 150 MHz broad filter cavities in series to filter out the strong optical driving pumps, which also filter the Stokes and anti-Stokes scattered photons within a frequency range of 80 MHz around the setpoint (4.98 GHz). In this way, any signal from the mechanical modes greater than 5.02 GHz is strongly suppressed, and hence only the part of the spectrum with the evenly spaced mechanical modes will contribute considerably to the correlation. These modes build a frequency comb with a free spectral range (FSR) of around 11 MHz, which corresponds to a rephasing time of  $1/\text{FSR} = 91$  ns. This is consistent with the round-trip time that can be inferred from the measurement, which is around 85 ns.

To verify that we can guide a non-classical mechanical state, we employ a scheme in which we herald the creation of a quantum excitation in the optomechanical cavity, which we confirm by swapping out the mechanical excitation to an optical photon after some time and correlating the photon statistics from the two processes<sup>29</sup>. We obtain these correlations by measuring the coincidences between the events on the SNSPDs. We realize this scheme by first addressing the Stokes process with a 119 fJ blue-detuned 40 ns laser pulse creating a two-mode squeezed optomechanical state with scattering probability of  $p_{s,\text{write}} \approx 1.4\%$ . Similarly, to read out the mechanical state from the optomechanical cavity, a red-detuned laser pulse with the same energy, duration and scattering probability of  $p_{s,\text{read}} \approx 1.4\%$  is sent to the device addressing the anti-Stokes process. These low values are chosen to avoid excess heating of the optomechanical device from the remaining optical absorption in the silicon. Note however that it has been shown that these can be increased up to around 30% (ref. 27). These scattering probabilities set the thermal occupation of the mode of interest to  $n_{\text{th}} \approx 0.27$  (see SI).

The scheme of the pulses can be seen in Fig. 3a, and the delay between the red-detuned and blue-detuned pulses is set to approximately the second round-trip time ( $\tau \approx 170$  ns). The detection of a single photon in one of the detectors from the blue-detuned pulse heralds the mechanical state of the defect to a single-phonon Fock state<sup>27</sup>. This phonon leaks through the attached phononic waveguide after a short time  $T_c$  and travels back and forth between the defect part and the end of the waveguide. In Fig. 2c, the highlighted area shows the chosen peak, which has a delay of  $\tau \approx 170$  ns, much smaller than the measured lifetime  $T_1 \approx 78 \mu\text{s}$  for this particular device (see the SI for more details). We choose to perform the

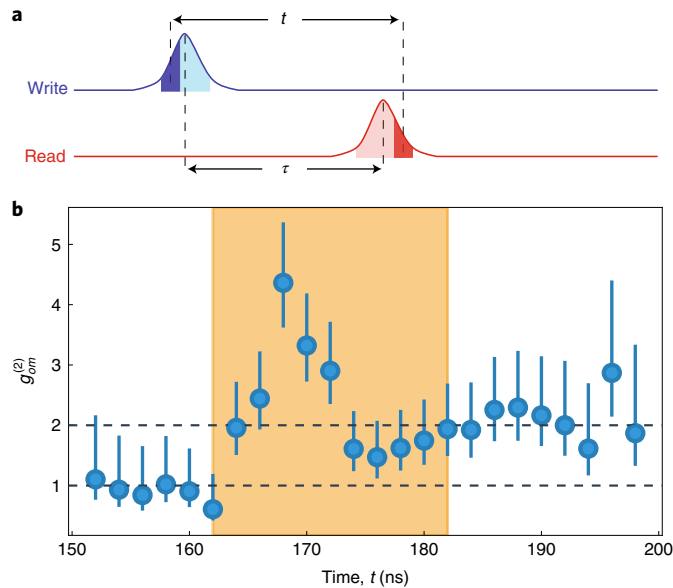


**Fig. 3 | Non-classical travelling phonons.** **a**, Pulse scheme used for the cross-correlation measurement. We fix the time between the pulses to  $\tau \approx 170$  ns, as calibrated from the measurement of Fig. 2c. In post-processing, we scan a narrow time window of 6 ns with an adjustable delay of  $t$  represented by the dark-blue and dark-red shaded areas over all of the acquired data (light-shaded areas). This approach allows us to calculate the  $g_{\text{om}}^{(2)}$  of each point with an adjustable moving window. **b**, Cross correlation between the optical and the mechanical state for the pulsed experiment  $g_{\text{om}}^{(2)}(t)$  (blue dots). The correlation is higher than the classical threshold of 2 (black dashed line), with a maxima of  $g_{\text{om}}^{(2)} = 4.4_{-0.7}^{+1.0}$ , clearly demonstrating the non-classical character of the travelling phonons. For more details on the error calculation, see the SI. The highlighted area in the figure has the same position as the one in Fig. 2c. The dashed line at 1 indicates uncorrelated events. The error bars are one standard deviation.

measurement after two round trips of the phonons to avoid any overlap between the optical write and read pulses. Another reason for this is to overcome the SNSPDs' dead time of around 100 ns and hence be able to measure coincidences on the same SNSPD as well as from different SNSPDs. Note that the expected cross-correlation between phonons and photons on multiple round trips is expected to be similar or slightly lower as a result of optical absorption and delayed heating<sup>27,29</sup>. From this measurement, we can also infer the coupling between the cavity and the waveguide from the width of the chosen peak, obtaining a decay time of  $T_c \approx 10$  ns, corresponding to a coupling rate of around  $2\pi \times 16$  MHz.

To measure the coincidences required to determine the correlations, two 6-ns-wide time windows, with a varying delay  $t$  between them, are scanned through the whole area of pulses in a post-processing step (Fig. 3a). Note that we also use the measurement shown in Fig. 2c to calibrate these filtering windows. By summing all the coincidences with each click happening in the same trial ( $\Delta n = 0$ , for  $n$  indicating each trial), we gather all the correlated coincidences for each delay. To obtain the average uncorrelated coincidences, we perform a similar post-processing step, but finding coincidences in different trials ( $\Delta n \neq 0$ ) where the clicks can be assumed to be uncorrelated. Averaging this value over different  $\Delta n \neq 0$  gives the average number of uncorrelated coincidences. We use these two values to calculate  $g_{\text{om}}^{(2)}(t)$ . The time window is chosen to be less than the coupling time between the cavity and the waveguide ( $T_c$ ) in order to select only the correlated photons that have indeed travelled in the waveguide (see SI for more details). The result is shown in Fig. 3b. To gather more statistics, two separate

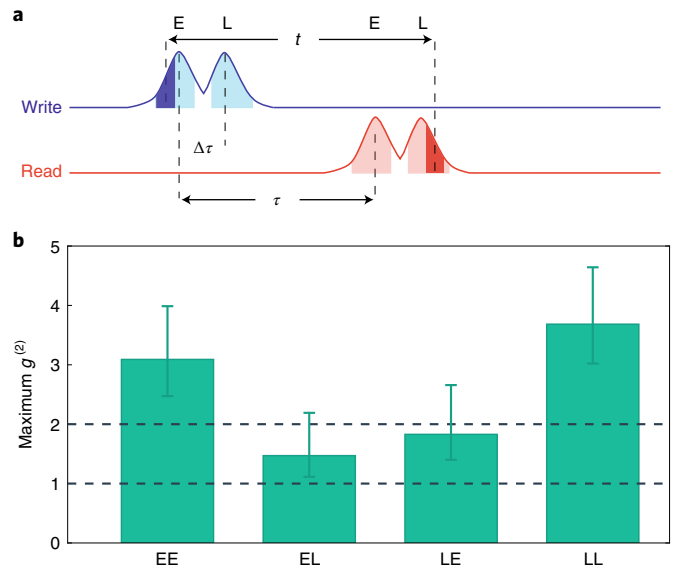


**Fig. 4 | Time-bin-encoded phonon states.** **a**, Pulse scheme for the generation of time-bin-encoded phonon states with  $\Delta\tau = 45$  ns and  $\tau = 170$  ns. The area used to gather coincidences is depicted by the light-blue (red) shaded area for the write (read) pulses, respectively. In the post-processing step, a similar technique as before is used, to achieve high timing resolution. An example of 6-ns-wide coincidence-filtering windows are sketched by dark-blue (dark-red) areas for write (read) pulses for the 'early-late' combination, where 'E' and 'L' stand for early and late, respectively. **b**, The maximum cross correlations for the various settings. As expected, they clearly show non-classical correlations for the 'early-early' and 'late-late' combinations, whereas in the other two we only observe classically correlated phonons. The dashed lines indicate the classical threshold (2) and uncorrelated events (1). Error bars are one standard deviation.

measurements with identical thermal occupation have been used for the data shown here, one with the sequence of red and blue pulses repeated every 200  $\mu\text{s}$  and the other every 300  $\mu\text{s}$ . After merging all the coincidences, a maximum cross correlation of  $g_{\text{om}}^{(2)} = 4.4_{-0.7}^{+1.0}$  is obtained from the reflected phonons at a time of  $t = 168$  ns, which is more than 3 s.d. above the classical threshold of 2, unambiguously showing the non-classical behaviour of the guided single-phonon state<sup>29</sup>. Furthermore, no non-classical correlations between the photons can be observed at times where the phonon is not spatially located inside the defect (that is, outside a window of width  $T_c$  centred at  $t \approx \tau \approx 170$  ns). We suspect the slightly increased correlations at longer times to be a result of the waveguide dispersion. This effect is also clearly visible in the envelope of the peak shape corresponding to the second round trip in the inset of Fig. 2c, with both patterns closely resembling one another.

We further explore the potential for creating a time-bin-encoded phononic state by extending our scheme to using two optical excitation (write) and two detection pulses (read), effectively realizing a phononic first-in first-out quantum memory<sup>32</sup>. The identical blue-detuned optical pulses (full-width at half-maximum 40 ns) have a scattering probability of  $p_{\text{s,write}} \approx 2.7\%$  with  $\Delta\tau = 45$  ns delay. The red-detuned detection pulses (full-width at half-maximum 40 ns) have a scattering probability of  $p_{\text{s,read}} \approx 1.5\%$  with the same time delay. The first blue- and red-detuned pulses are spaced by  $\tau = 170$  ns from each other, and we repeat this sequence every 800  $\mu\text{s}$ . We then measure the maximum cross correlation in time between all four combinations of write and read pulses, using the same technique for delay filtering as used to extract the data shown

in Fig. 3. We choose 40-ns-long non-overlapping time windows to separate ‘early’ write and read pulses from ‘late’ ones, as depicted in Fig. 4a. As shown in Fig. 4b, we can clearly see strong non-classical correlation between the ‘early–early’ and ‘late–late’ combination of excitation and detection pulse, while observing only classical correlations (due to absorption-induced heating) between the other combinations of ‘early–late’ and ‘late–early’.

Our results clearly demonstrate the potential for creating, guiding and detecting a non-classical mechanical state inside a phononic crystal, using optomechanical techniques. Thanks to the long mechanical lifetime (up to 5.5 ms for similar devices on the same chip) and the full lateral confinement, this type of device paves the way towards on-chip quantum acoustic experiments. The current efficiency of the device is limited by residual optical absorption in the silicon, which can be reduced through improved fabrication<sup>27</sup> and surface passivation<sup>33</sup>. While some of the motivation for these experiments stems from the similarity to quantum optics, phonons are crucially different, due to the five orders of magnitude smaller propagation speed and the ease of coupling them to other quantum systems. The realization of phononic beamsplitters and phase modulators will complete the toolbox required for full control over travelling single phonons and more complex quantum experiments on a chip. Furthermore, the possibility of retrieving the state after several round trips and of having time-bin-encoded phononic states, together with the full engineerability of the band structure, will allow for the creation of time-bin-encoded phononic qubits and an optomechanical multimode quantum memory working natively at telecommunications wavelengths. We also expect guided phonon modes to play a crucial role in the low-energy transmission of quantum information on a chip and for next-generation filtering.

### Online content

Any methods, additional references, Nature Research reporting summaries, source data, extended data, supplementary information, acknowledgements, peer review information; details of author contributions and competing interests; and statements of data and code availability are available at <https://doi.org/10.1038/s41567-022-01612-0>.

Received: 2 September 2021; Accepted: 10 April 2022;  
Published online: 23 May 2022

### References

- Aspelmeyer, M., Kippenberg, T. J. & Marquardt, F. Cavity optomechanics. *Rev. Mod. Phys.* **86**, 1391 (2014).
- O’Connell, A. D. et al. Quantum ground state and single-phonon control of a mechanical resonator. *Nature* **464**, 697–703 (2010).
- Palomaki, T., Teufel, J., Simmonds, R. & Lehnert, K. Entangling mechanical motion with microwave fields. *Science* **342**, 710 (2013).
- Riedinger, R. et al. Remote quantum entanglement between two micromechanical oscillators. *Nature* **556**, 473–477 (2018).
- Ockeloen-Korppi, C. F. et al. Stabilized entanglement of massive mechanical oscillators. *Nature* **556**, 478–482 (2018).
- Marinković, I. et al. An optomechanical Bell test. *Phys. Rev. Lett.* **121**, 220404 (2018).
- Wallucks, A., Marinković, I., Hensen, B., Stockill, R. & Gröblacher, S. A quantum memory at telecom wavelengths. *Nat. Phys.* **16**, 772–777 (2020).

- Andrews, R. W. et al. Bidirectional and efficient conversion between microwave and optical light. *Nat. Phys.* **10**, 321–326 (2014).
- Vainsencher, A., Satzinger, K. J., Peairs, G. A. & Cleland, A. N. Bi-directional conversion between microwave and optical frequencies in a piezoelectric optomechanical device. *Appl. Phys. Lett.* **109**, 033107 (2016).
- Forsch, M. et al. Microwave-to-optics conversion using a mechanical oscillator in its quantum groundstate. *Nat. Phys.* **16**, 69–74 (2020).
- Mirhosseini, M., Sipahigil, A., Kalaee, M. & Painter, O. Superconducting qubit to optical photon transduction. *Nature* **588**, 599–603 (2020).
- Habraken, S. J. M., Stannigel, K., Lukin, M. D., Zoller, P. & Rabl, P. Continuous mode cooling and phonon routers for phononic quantum networks. *N. J. Phys.* **14**, 115004 (2012).
- Delsing, P. et al. The 2019 surface acoustic waves roadmap. *J. Phys. D* **52**, 353001 (2019).
- Schuetz, M. J. A. et al. Universal quantum transducers based on surface acoustic waves. *Phys. Rev. X* **5**, 031031 (2015).
- Bienfait, A. et al. Phonon-mediated quantum state transfer and remote qubit entanglement. *Science* **364**, 368 (2019).
- Golter, D. A. et al. Coupling a surface acoustic wave to an electron spin in diamond via a dark state. *Phys. Rev. X* **6**, 041060 (2016).
- Hermelin, S. et al. Electrons surfing on a sound wave as a platform for quantum optics with flying electrons. *Nature* **477**, 435–438 (2011).
- McNeil, R. P. G. et al. On-demand single-electron transfer between distant quantum dots. *Nature* **477**, 439–442 (2011).
- Kuzyk, M. C. & Wang, H. Scaling phononic quantum networks of solid-state spins with closed mechanical subsystems. *Phys. Rev. X* **8**, 041027 (2018).
- Chu, Y. & Gröblacher, S. A perspective on hybrid quantum opto- and electromechanical systems. *Appl. Phys. Lett.* **117**, 150503 (2020).
- Gustafsson, M. V., Santos, P. V., Johansson, G. & Delsing, P. Local probing of propagating acoustic waves in a gigahertz echo chamber. *Nat. Phys.* **8**, 338–343 (2012).
- Gustafsson, M. V. et al. Propagating phonons coupled to an artificial atom. *Science* **346**, 207 (2014).
- Patel, R. N. et al. Single-mode phononic wire. *Phys. Rev. Lett.* **121**, 040501 (2018).
- Fang, K., Matheny, M. H., Luan, X. & Painter, O. Optical transduction and routing of microwave phonons in cavity-optomechanical circuits. *Nat. Photon.* **10**, 489–496 (2016).
- Farrera, P., Heinze, G. & De Riedmatten, H. Entanglement between a photonic time-bin qubit and a collective atomic spin excitation. *Phys. Rev. Lett.* **120**, 100501 (2018).
- Chan, J., Safavi-Naeini, A. H., Hill, J. T., Meenehan, S. & Painter, O. Optimized optomechanical crystal cavity with acoustic radiation shield. *Appl. Phys. Lett.* **101**, 081115 (2012).
- Hong, S. et al. Hanbury Brown and Twiss interferometry of single phonons from an optomechanical resonator. *Science* **358**, 203 (2017).
- Qiu, L., Shomroni, I., Seidler, P. & Kippenberg, T. J. Laser cooling of a nanomechanical oscillator to its zero-point energy. *Phys. Rev. Lett.* **124**, 173601 (2020).
- Riedinger, R. et al. Non-classical correlations between single photons and phonons from a mechanical oscillator. *Nature* **530**, 313–316 (2016).
- Weis, S. et al. Optomechanically induced transparency. *Science* **330**, 1520 (2010).
- Meenehan, S. M. et al. Silicon optomechanical crystal resonator at millikelvin temperatures. *Phys. Rev. A* **90**, 011803 (2014).
- Pang, X.-L. et al. A hybrid quantum memory-enabled network at room temperature. *Sci. Adv.* **6**, eaax1425 (2020).
- Borselli, M., Johnson, T. J. & Painter, O. Measuring the role of surface chemistry in silicon microphotonic. *Appl. Phys. Lett.* **88**, 131114 (2006).

**Publisher’s note** Springer Nature remains neutral with regard to jurisdictional claims in published maps and institutional affiliations.

© The Author(s), under exclusive licence to Springer Nature Limited 2022

### Data availability

Source data for the plots are available on Zenodo via <https://doi.org/10.5281/zenodo.6384236>. Source data are provided with this paper.

### Acknowledgements

We thank E. Verhagen and R. Burgwal for valuable discussions and M. Forsch for experimental support. We further acknowledge assistance from the Kavli Nanolab Delft. This work is financially supported by the European Research Council (ERC CoG Q-ECHOS, 101001005), and by the Netherlands Organization for Scientific Research (NWO/OCW), as part of the Frontiers of Nanoscience programme, as well as through Vidi (680-47-541/994) and Vrij Programma (680-92-18-04) grants. R.S. also acknowledges funding from the European Union under a Marie Skłodowska-Curie COFUND fellowship.

### Author contributions

A.Z., R.S. and S.G. devised and planned the experiment. A.Z. simulated, designed and fabricated the sample. A.Z., R.S. and N.F. built the setup and performed the

measurements. All authors analysed the data and wrote the manuscript. S.G. supervised the project.

### Competing interests

The authors declare no competing interests.

### Additional information

**Supplementary information** The online version contains supplementary material available at <https://doi.org/10.1038/s41567-022-01612-0>.

**Correspondence and requests for materials** should be addressed to Simon Gröblacher.

**Peer review information** *Nature Physics* thanks Krishna Balram and the other, anonymous, reviewer(s) for their contribution to the peer review of this work.

**Reprints and permissions information** is available at [www.nature.com/reprints](http://www.nature.com/reprints).